2010 IEEE International Conference on Robotics and Automation
Anchorage Convention District
May 3-8, 2010, Anchorage, Alaska, USA

Three-Axis Micro-Force Sensor with Tunable Force Range and Sub-Micronewton Measurement Uncertainty

S. Muntwyler, *Student Member, IEEE*, F. Beyeler, *Member, IEEE*, and B.J. Nelson, *Member, IEEE*

***Abstract*—This paper presents the design, fabrication and characterization of the first microfabricated three-axis tunable force sensor with sub-micronewton measurement uncertainty. The sensing range can be electrically tuned from +/-20 μN to +/-200 μN while taking measurements, ensuring optimal sensor characteristics for a large variety of applications. Since the sensor has been pre-calibrated for the entire tuning range the exact sensor gain and its uncertainty is known. Real-time, three degree of freedom force feedback makes this sensor a valuable tool for micromanipulation.**

I. Introduction

MICROROBOTIC manipulation of objects with dimensions in the micro- to nanonewton range has received increasing interest in the past decade leading to the development of novel tools with application in a variety of emerging field of research. In general, visual feedback is solely available to observe the interactions of the sample and the manipulator allowing only highly skilled and specially trained users to perform these tasks. MEMS (Micro-Electro-Mechanical Systems) force sensors enables the measurement of these interaction forces. These MEMS sensors have also become a valuable tool in other fields, such as material science and mechanobiology, allowing a quantitative measurement of mechanical properties of micrometer sized samples [1]. They are also used to measure the effect of forces on biological samples, such as described in [2], where the touch sensitivity of C.elegans is measured giving insight into the conversion of mechanical forces into electrochemical signals.

The most common example of such a force sensor is the widely used atomic force microscope (AFM), based on measuring the deflection of a cantilever either by an optical beam or piezoresistive material. This technique is limited to a very narrow force range and, in most cases, to measurements in one degree of freedom (DOF). For many applications multi-axis sensing offers a great advantage e.g. in the case of automated cell injection [3], since a misalignment of the cell and the injection pipette can be detected and corrected for. A variety of multi-axis force sensors based on different principles have been developed and successfully used to gather quantitative force data in a variety of applications [4-7]. But none of them offer sub-micronewton resolution.

The forces dominating in micromanipulation range from tens of nanonewtons (10^{-9} N) up to hundreds of micronewtons (10^{-6} N) [8]. Therefore, it is desirable to have a single sensor capable of measurements in this entire force range. Additionally, little work has been published on the calibration of multi-axis micro-force sensors and their uncertainty analysis. The results obtained from a sensor are only complete when accompanied by a statement of uncertainty, indicating their quality.

This paper presents the design, fabrication and characterization of the first microfabricated three-axis tunable force sensor with sub-micronewton measurement uncertainty. The force range can be electronically tuned from +/-20 μN to +/-200 μN with a highest resolution of 30 nN. Sensor calibration, the most important sensor characteristics, and their influence on measurement uncertainty are presented. Finally, a novel microfabrication process is described enabling a major reduction in the fabrication complexity of multi-axis sensors and actuators.

II. Working Principle

The force sensor consists of a movable body with attached probe suspended by flexures within an outer frame. A force applied to the probe results in a relative motion of the body and the frame, which can be measured by capacitive

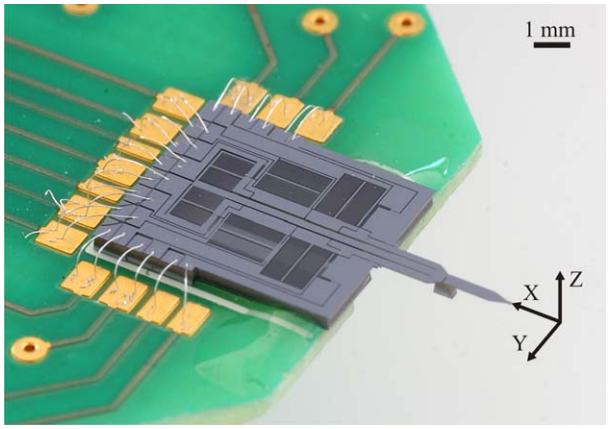

Fig. 1. MEMS-based capacitive three-axis micro-force sensor. The sensor dimensions without the sensor probe are 5 by 6 mm and the probe length is 3 mm.

Manuscript received September 15, 2009. This work is conducted with financial support from the project "Hybrid Ultra Precision Manufacturing Process Based on Positional and Self-assembly for Complex Micro-Products (HYDROMEL)" funded by the European Commission under the 6th Framework Program (FP6).

S. Muntwyler, F. Beyeler and B.J. Nelson are with the ETH Zurich, Zurich, CH 8092 Switzerland (msimon@ethz.ch, fbey@ethz.ch, bnelson@ethz.ch).

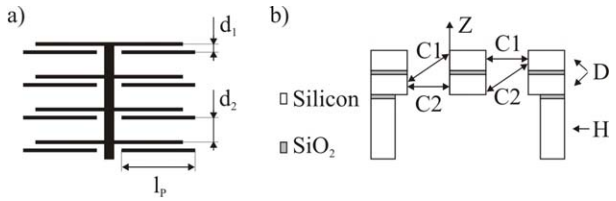

Fig. 2. (a) Geometry of the sensing capacitor array (comb drive). (b) Cross-section of the out-of-plane sensing capacitor.

electrodes as a change of capacitance. Allowing the sensor to move in multiple directions and by using several of these capacitive displacement sensors, forces in multiple axes can be measured. A photograph of the sensor is displayed in Fig. 1. This work focuses on capacitive force sensing because of its low sensitivity to changes in environmental conditions, such as light, temperature and humidity. The capacitive electrodes are arranged as parallel plate capacitor arrays (comb drives) as shown in Fig. 2a, enabling them to measure displacements in two configurations: transversely, through a change in the gap width *d* between the capacitor plates and laterally, through a change in the overlapping area of the capacitor plates. The transversal way offers very high sensitivity but a lack of linearity, which can be overcome by differentially measuring two capacitive changes in opposite directions. The sensor output is then proportional to the difference in capacitance. More details about capacitive sensing can be found in [9]. Forces in the sensor plane (x and y) are measured transversely with two capacitor pairs. However, due to the planar MEMS based fabrication, forces or displacements out of the sensor plane (z-direction) need to be measured laterally. A cross-section of the z-axis sensing capacitor configuration is shown in Fig 2b. The sensor is fabricated based on a double silicon-on-insulator (SOI) substrate. The relatively thick silicon handle layer (H) forms the outer frame of the sensor whereas the two thin silicon device layers (D) form the active elements and the moveable body. All the layers are electrically isolated by a silicon dioxide (SiO_2) layer. A single device layer is sufficient to measure displacements in three DOF, but the additional layer enables the distinction between positive and negative forces. In this case the differential capacitance *C1-C2* is negative when the inner sensing body moves up ($Z > 0$) and positive when it moves down ($Z < 0$). The schematic of the sensor is shown in Fig. 3. Due to the unequal sensitivity of transversal in-plane sensing compared to lateral out-of-plane sensing, these degrees of freedom are

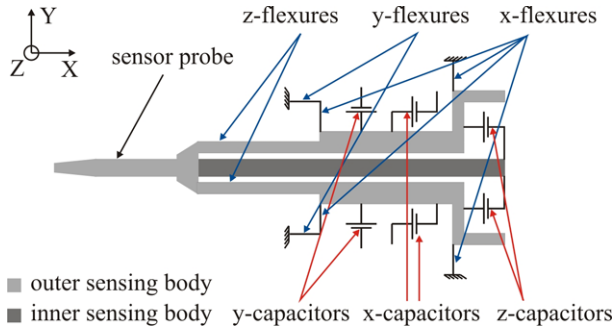

Fig. 3. Three-axis micro-force sensor schematic.

TABLE I
SENSING CAPACITOR DIMENSIONS

	x-axis and y-axis capacitor	z-axis capacitor
d1	7 μm	7 μm
d2	20 μm	7 μm
l_P	500 μm	500 μm
t	50 μm	25 μm
n	60	50

divided into two sensing bodies suspended within each other. The outer body measures displacements in x and y (and therefore forces relative to them) and the inner sensing body displacements (forces) relative to the outer sensing body in z. The dimensions of the sensing comb drives are listed in Table I, where *n* is the number of capacitor plate pairs and *t* the thickness of the capacitive electrodes.

III. SENSOR DESIGN

The sensor is designed to measure forces of up to 200 μN in x, y and z. Multiple sensor configurations (position and geometry of flexures, capacitors and movable bodies) have been analytically compared. Besides the sensitivity criterion for each axis the most important factor in multi-axis sensor design is the decomposability of the force components. To ensure a minimum cross-coupling between the different axes each capacitor pair is dedicated to a single force component and placed such that the main contribution to an output signal can be directly related to the force in the corresponding direction. Therefore, the x-capacitor is mainly sensitive to forces in x, the y-capacitor to forces in y and the z-capacitor to forces in z. Similar considerations have been made for the flexures such that by changing the dimensions

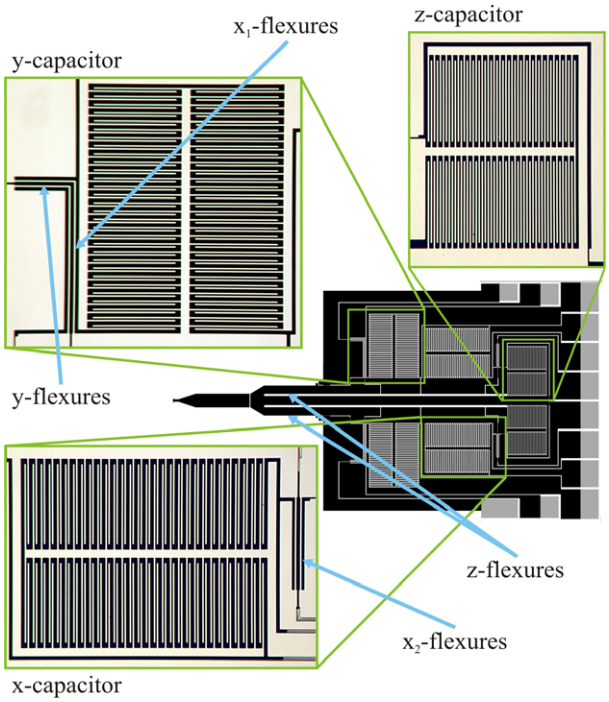

Fig. 4. Close-up views of the micro-force sensor.

of the flexures the mechanical stiffness of the sensor can be independently adjusted for each axis.

Due to the lower sensitivity of the lateral sensing principle, forces in z need to produce a much larger deflection of the capacitor electrodes than forces in x or y. Therefore, the inner sensing body is designed as an amplification lever, shown in Fig. 3, and the z-capacitor is placed as far from the sensor tip as possible to maximize its leverage effect.

An ANSYS finite element model (FEM) has been created to calculate the quantitative mechanical response of the sensor to an applied force at its probe. This enables the optimization of the flexure geometry for a certain target sensitivity along the three axes. The deflections at the position of each capacitor and the corresponding differential signal change were used as the design criteria and the flexure dimensions as the design parameter. Using the FEM analysis in an optimization loop, starting with an initial estimate of the flexure dimensions, the difference from the target deformations in each capacitor and for each force direction where found. By scaling the flexure dimensions with these errors, the ideal flexure geometry could be found, not only ensuring the desired signal change at the target force in the corresponding capacitor pair, but also minimizing the signals in all the other capacitor pairs. The resulting flexures are shown in Fig. 4. Since all the capacitors need to have electrical contact to the outer frame, two flexures at each point had to be fabricated instead of one to produce the required electrical connections.

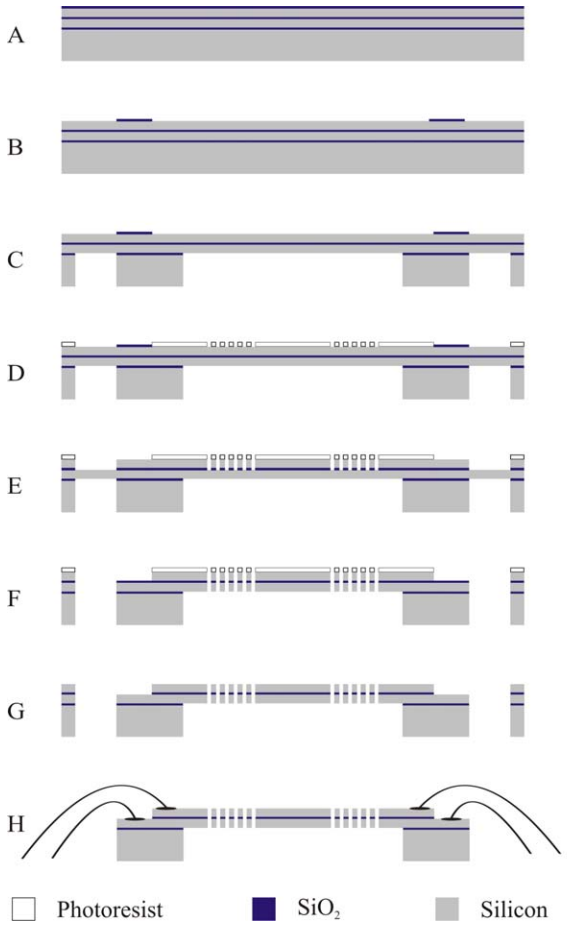

Fig. 5. Sensor micro-fabrication process.

IV. Fabrication

The force sensors are fabricated by a MEMS-based bulk silicon microfabrication process. In [6] a three-mask process based on an SOI substrate describes the fabrication of sensors measuring deflections in the sensor plane. In [7] a more complex five mask fabrication process including wafer-bonding is presented, enabling the measurement of in- and out-of-plane displacements.

In this work a three-mask process has been developed, similar in complexity to the SOI process published in [6], but enabling three-axis sensors or actuators. It is based on a double SOI substrate with sequential etching of the two device layers by dry etching. Wafer bonding is not required. Even though the double SOI substrates are more expensive, the reduction of photomasks and fabrication steps results in a higher yield rate and, therefore, in a more efficient fabrication. In Fig. 5 the fabrication process is depicted. The photoresist layers are only shown in the steps involved in the sequential etching of the two device layers (D-F).

A) A 100 mm diameter double SOI wafer is used as a substrate, with a handle layer thickness of 400 µm, two device layers with a thickness of 25 µm and three SiO_2 layers with a thickness of 2 µm. All silicon layers have a <100> orientation and are highly p-doped.

B) The SiO_2 on the top device layer is structured with reactive ion etching (RIE) to form an etch mask in the regions, where in the last step, wires are bonded to the lower device layer.

C) The handle layer is etched by deep reactive ion etching (DRIE) where the SiO_2 acts as an etch stop and is removed subsequently by RIE. This will form the outer frame of the sensors. Since the sensor features a probe overhanging the rest of the device, dicing cannot be done to separate the individual dies. Therefore, a cavity surrounding the sensor is etched in this step.

D) The photoresist (AZ 4562) is applied with a thickness of 5 µm and structured to form a second etch mask on the top device layer. This defines the active parts of the sensor like comb drives, flexures and the movable bodies.

E) The wafer is mounted onto a support wafer, and the top device layer is etched by DRIE. Subsequently the underlying SiO_2 is etched by RIE. The SiO_2 etch mask, formed in A, is removed during this step as well.

F) The lower silicon device layer is structured by DRIE with the same photoresist mask, completely releasing the devices. At the same time the top device layer is etched in the regions where the SiO_2 mask was removed in step E.

G) The SiO_2 on the lower bonding regions is removed by

RIE and the remaining photoresist striped in oxygen plasma.

H) In the last step the sensors are glued onto a circuit board and wire bonded.

V. Readout Electronics

The electronic readout of the sensing capacitance is based on the impedance relation measurement where two periodic, 180° phase-shifted excitation voltages are applied to a capacitor pair. The demodulated response of the common electrode is then proportional to the ratio of the two capacities [6]. A commercial capacitance-to-voltage converter IC (CVC1.1, GEMAC) is used to interface each capacitor pair (*C1* and *C2*) on the sensor. This mixed signal integrated circuit consists essentially of a charge integrator with integration capacitance C_{int}, a sample hold cell, a second order low-pass filter, where the cut-off frequency has been set to 5 kHz, and an amplifier stage with an additional gain that can be set by a serial interface. The analog part of the block diagram of the readout is shown in Fig. 6. Since the sensor is designed to measure positive and negative forces, all the internal operational amplifiers and the output voltage are trimmed to the midpoint of their range of 0 V to 4 V, so forces will result in maximum voltage changes of +/- 2 V. All the settings are stored in an integrated EEPROM cell. The serial interface and the analog voltage readout have been realized using Labview and a data acquisition card (NI PCI-6259). By changing the values of C_{int} and *Gain*, shown in (1), the sensitivity of the sensor can be electronically tuned to the appropriate force range of the specific application.

$$V_{out} \propto Gain \cdot \frac{C1 - C2}{C_{int}} \tag{1}$$

VI. Sensor Characterization

A. Calibration

The most commonly used micro-force sensor, the AFM, has led to the development of a large number of methods to calibrate forces in the micro- and nanonewton range [10]. However, the accuracy of these methods is unknown since none of them are traceable to SI units. The unit force is derived from the definition of newton using a combination of base SI units (kg, m and s) [11].

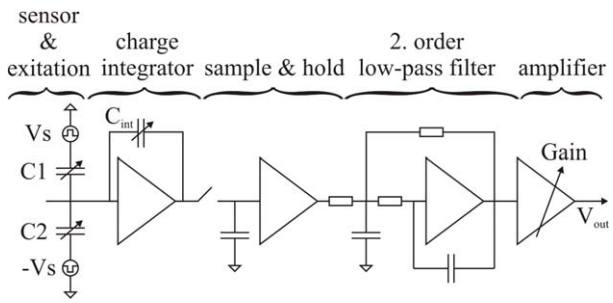

Fig. 6. Block diagram of the capacity-to-voltage converter (CVC 1.1).

Increasing effort is being made in multiple national measurement institutes (NMI) to create an SI traceable reference standard for the calibration of small forces. An overview of the different approaches can be found in [11]. However, when calibrating samples pre-calibrated by another NMI, even NMI's show differences of up to 30 % in the results [12]. Currently there is no commercial, SI traceable reference force sensor system in the micro- and nanonewton range available. Therefore, in this work, no claim is made of absolute accuracy in the calibration performed. For the calibration, as a comparison of the sensor with another standard, a commercially available, calibrated micro-force sensor (FT-S540, Femtotools) is used as a reference and the uncertainty analysis is carried out relative to this. To obtain the calibration matrix $\boldsymbol{A}^{3x3}$, which describes the relationship between the output voltages $\boldsymbol{V}$ = *(Vx Vy Vz)* of the sensor and the applied forces $\boldsymbol{F}$ = *(Fx Fy Fz)*, forces in all directions (x, y and z) are subsequently applied to the sensor probe.

$$\mathbf{F} = \mathbf{V} \cdot \mathbf{A} \tag{2}$$

The resulting calibration output voltage signals $\boldsymbol{V_C}$ are compared with the force signals $\boldsymbol{F_C}$ from the reference. By using the least square method (4), minimizing the residual $\boldsymbol{r}$, the best estimate of the calibration Matrix $\hat{\boldsymbol{A}}$ is found. To facilitate the understanding of the uncertainty analysis, shown in the next section, the system of equations is divided into three systems.

$$\mathbf{F}_c = \mathbf{V}_c \cdot \hat{\mathbf{A}} + \mathbf{r}_{\min} \tag{3}$$

$$\hat{\mathbf{A}}_j = \left(\mathbf{V}_c{}^T \cdot \mathbf{V}_c\right)^{-1} \cdot \mathbf{V}_c{}^T \cdot \mathbf{F}_{j,c} \quad \text{with } j = x, y, z \tag{4}$$

$$\hat{\mathbf{A}} = \left[\hat{\mathbf{A}}_x \quad \hat{\mathbf{A}}_y \quad \hat{\mathbf{A}}_z\right] \tag{5}$$

B. Sensor characteristics and uncertainty

The result of a measurement is only an approximation of the value of the measurand and, thus, is complete only when accompanied by a statement of the uncertainty of that estimate [13]. The measurement uncertainty is a parameter associated with the results of a measurement that characterizes the dispersions of the values that could reasonably be attributed to the measurand [14]. Therefore, besides the calibration matrix and the corresponding sensing range, the most important characteristics of the sensor are measured and their influence onto the measurement uncertainty calculated.

Force range: The maximum measurable force can be found by multiplying the calibration matrix with the maximum voltage change in all axes (2 V).

Resolution: The smallest force increment that can be detected, limited by the noise in the sensor output. The uncertainty in the force measurement due to noise ($\mathbf{u}_{\text{Noise}}$)

is given by the standard deviation of the output voltages multiplied by the calibration matrix.

Sensor drift: The change in the output signal without any change of the applied force over a certain time period. The uncertainty due to drift is calculated using (6), the root mean square of the voltage change ΔV in the time period t (10 s), where n is the number of intervals measured over.

$$u_{\mathrm{Drift,j}}(t) = \sqrt{\frac{\sum \Delta \mathbf{V}(t)^2}{n-1}} \cdot \hat{\mathbf{A}}_j \tag{6}$$

Uncertainties in the calibration matrix: All sources of uncertainties related to the calibration matrix, such as cross-sensitivity and non-linearity are combined into the uncertainty in the force prediction, as shown in (7). It is calculated using the covariance matrix in (8) and the mean square error δ_j^2 in (9), where k is the number of calibration data points.

$$u_{\mathrm{Pred.},j} = \sqrt{\delta_j{}^2 + \mathbf{V}_p \cdot Var\left(\hat{\mathbf{A}}_j\right) \cdot \mathbf{V}_p{}^T} \tag{7}$$

$$Var\left(\hat{\mathbf{A}}_j\right) = \delta_j{}^2 \cdot \left(\mathbf{V}_c{}^T \mathbf{V}_c\right)^{-1} \tag{8}$$

$$\delta_j{}^2 = \frac{\left(\mathbf{F}_{jc} - \hat{\mathbf{F}}_j\right)^T \left(\mathbf{F}_{jc} - \hat{\mathbf{F}}_j\right)}{k-3} \text{ with } \hat{\mathbf{F}}_j = \mathbf{V}_c \cdot \hat{\mathbf{A}}_j \tag{9}$$

Expanded combined uncertainty: By combining all the sources of measurement uncertainty together and multiplying them with the coverage factor k, the expanded combined uncertainty can be calculated as shown in (10). Utilizing the central limit theorem a normal distribution is assumed, and, therefore, a coverage factor of 1 or 2 will result in a confidence level of approximately 68 % or 95 %, respectively.

$$\mathbf{u} = k \cdot \sqrt{\mathbf{u}_{Drift}{}^2 + \mathbf{u}_{Noise}{}^2 + \mathbf{u}_{\mathrm{Pred.}}{}^2} \tag{10}$$

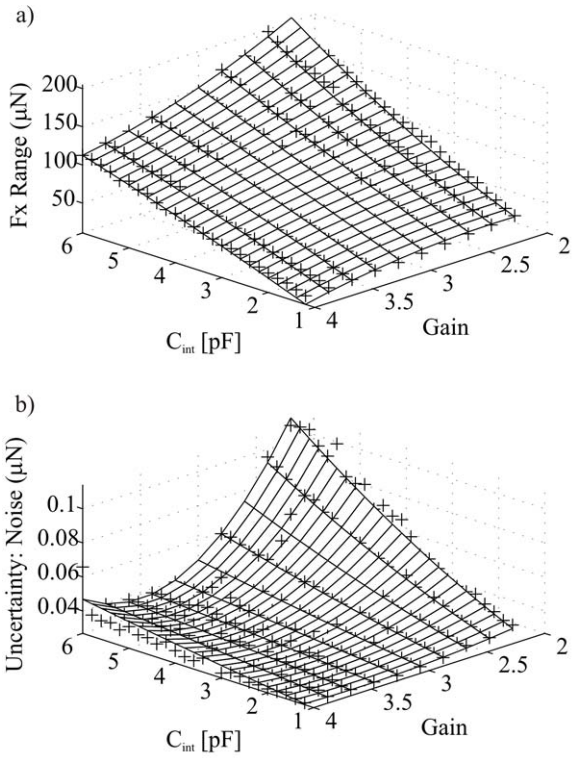

Fig. 7. Sensor characteristics in function of C_{int} and *Gain*. (a) Force range *Fx*. (b) Uncertainty in the force *Fx* due to noise.

C. *Sensor tuning and corresponding characteristics*

Depending on the application, a specific force range is required. By tuning the range of the sensor, the ideal sensor characteristics and the smallest possible measurement uncertainties can be guaranteed. Therefore, the sensor is characterized for a number of different settings of the readout electronics. The integrator capacitance C_{int} has been varied from 1.2 pF to 6.0 pF in 0.2 pF steps and the amplifier gain from 2.2 to 4.0 in 0.2 steps. For each combination of these two parameters the sensor has been calibrated five times along each axis, the sensor characteristics have been recorded, and the corresponding measurement uncertainties calculated. The force range and the uncertainty due to noise for x, from a total of 3750

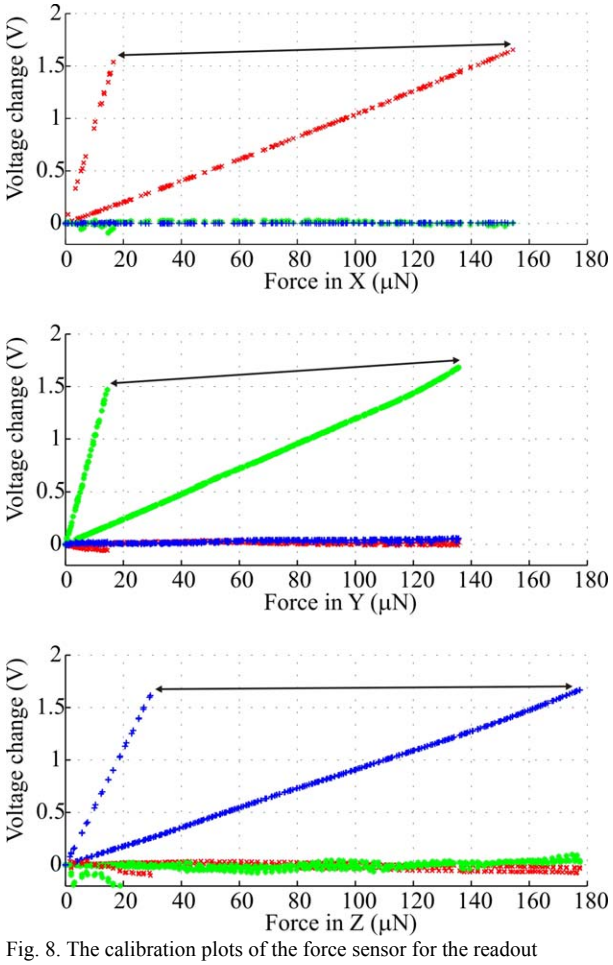

Fig. 8. The calibration plots of the force sensor for the readout settings shown in Table II. The raw calibration data for *Vx* are x, for *Vy* are * and *Vz* are +.

TABLE II
SENSOR CHARACTERISTICS

Gain	4	3
C_{int} (pF)	1.2	2.2
A (μN/V)	$\begin{bmatrix} 10.80 & 0.39 & -2.12 \\ 0.24 & 9.89 & 0.80 \\ -0.04 & -0.24 & 18.44 \end{bmatrix}$	$\begin{bmatrix} 95.61 & -0.42 & -0.20 \\ -1.11 & 83.43 & -3.50 \\ -2.12 & -0.02 & 109.18 \end{bmatrix}$
Sensing Range (μN)		
Fx	+/- 22	+/- 192
Fy	+/- 20	+/- 176
Fz	+/- 31	+/- 222
Uncertainty: Noise at 10 Hz (μN)		
X	0.03	0.11
Y	0.03	0.07
Z	0.05	0.12
Uncertainty: Drift over 10 s (μN)		
X	0.01	0.04
Y	0.01	0.04
Z	0.02	0.07
Uncertainty: Prediction (μN)		
X	0.17 - 0.20	4.46 – 4.51
Y	0.23 - 0.26	4.69 – 4.75
Z	0.09 - 0.10	2.54 – 2.57

calibrations, can be seen in Fig. 7. The raw data are shown as + whereas the surface plots show a fit using a second-order polynomial in two variables, fitted using a least squares algorithm.

Using this setting range the force range of the sensor can be changed from approximately +/-20 μN to +/-200 μN. The calibration curves for the minimum and maximum sensor range are shown in Fig. 8. The arrows between the main components, which correlate to the diagonal elements in the calibration matrix, indicate the range in which the calibration curves can be adjusted. The corresponding uncertainty components are shown in Table II. The non-diagonal entries in the calibration matrix are almost zero, which can be verified in the calibration plots. This is an indication that the goal, to mechanically decompose the forces, has been successfully realized. Depending on the application and the range of forces needed to be measured, the sensor can now be electronically tuned during the measurements to the appropriate sensor range, since it has been characterized for all the settings in advance.

VII. CONCLUSION

An electronically tunable three-axis micro-force sensor, its design, fabrication and characterization has been presented. It has been designed such that cross-sensitivities and additional uncertainties related to cross-sensitivity are reduced. The sensor enables force measurements in a range between +/-20 μN and +/-200 μN with the best resolution down to 30 nN. Due to the unavailability of a commercial, SI traceable reference force sensor in the micro- and nanonewton range, the measurement uncertainties have been evaluated relative to a reference force sensor in the 0.1 μN range at the highest resolution. The main contributions of this work are:

- The first three-axis micro-force sensor enabling sub-micronewton force measurements.
- A tunable force range, enabling the sensor to be optimized for an application while measuring.
- A novel three-mask fabrication process enabling the fabrication of three-axis transducers with a major reduction in fabrication complexity.

REFERENCES

[1] Y. Sun and B. J. Nelson, "MEMS capacitive force sensors for cellular and flight biomechanics," Biomedical Materials, vol. 2, pp. S16-S22, Mar 2007.

[2] J. C. Doll, S. Muntwyler, F. Beyeler, S. Geffeney, M. B. Goodman, B. J. Nelson, B. L. Pruitt, "Measuring Thresholds for Touch Sensation in C. Elegans", Proc. in the 5th International Conference on Microtechnologies in Medicine and Biology (MMB), Québec, Canada, April 2009.

[3] Y. Sun, B. J. Nelson, D. P. Potasek, and E. Enikov, "A bulk microfabricated multi-axis capacitive cellular force sensor using transverse comb drives," Journal of Micromechanics and Microengineering, vol. 12, pp. 832-840, Nov 2002.

[4] A. Tibrewala, A. Phataralaoha, and S. Buttgenbach, "Simulation, fabrication and characterization of a 3D piezoresistive force sensor," Sensors and Actuators a-Physical, vol. 147, pp. 430-435, Oct 3 2008.

[5] A. Sieber, et al., "A novel haptic platform for real time bilateral biomanipulation with a MEMS sensor for triaxial force feedback," Sensors and Actuators a-Physical, vol. 142, pp. 19-27, Mar 10 2008.

[6] F. Beyeler, et al., "Design and calibration of a MEMS sensor for measuring the force and torque acting on a magnetic microrobot," Journal of Micromechanics and Microengineering, vol. 18, pp. -, Feb 2008.

[7] F. Beyeler, S. Muntwyler, and B. J. Nelson, "A Six-Axis MEMS Force-Torque Sensor With Micro-Newton and Nano-Newtonmeter Resolution," Journal of Microelectromechanical Systems, vol. 18, pp. 433-441, Apr 2009.

[8] F. Arai, D. Ando, T. Fukuda, Y. Nonoda, and T. Oota, "Micro manipulation based on micro physics - Strategy based on attractive force reduction and stress measurement," Iros '95 - 1995 Ieee/Rsj International Conference on Intelligent Robots and Systems: Human Robot Interaction and Cooperative Robots, Proceedings, Vol 2, pp. 236-241, 1995.

[9] Y. Sun, S. N. Fry, D. P. Potasek, D. J. Bell, and B. J. Nelson, "Characterizing fruit fly flight behavior using a microforce sensor with a new comb-drive configuration," Journal of Microelectromechanical Systems, vol. 14, pp. 4-11, Feb 2005.

[10] N. A. Burnham, et al., "Comparison of calibration methods for atomic-force microscopy cantilevers," Nanotechnology, vol. 14, pp. 1-6, Jan 2003.

[11] J. R. Pratt, J. A. Kramar, D. B. Newell, and D. T. Smith, "Review of SI traceable force metrology for instrumented indentation and atomic force microscopy," Measurement Science & Technology, vol. 16, pp. 2129-2137, Nov 2005.

[12] R. S. Gates and J. R. Pratt, "Prototype cantilevers for SI-traceable nanonewton force calibration," Measurement Science & Technology, vol. 17, pp. 2852-2860, Oct 2006.

[13] ISO, "Guide to the expression of uncertainty in measurement," Geneva, Switzerland, 1995.

[14] ISO, "International Vocabulary of Basic and General Terms in Metrology," Geneva, Switzerland, 1993.